Hot deformation behavior and flow stress modeling of Ti–6Al–4V alloy produced via electron beam melting additive manufacturing technology in single -phase field

(Article begins on next page)

16 July 2022

Hot Deformation Behavior and Flow Stress Modeling of Ti-6Al-4V Alloy Produced via Electron Beam Melting Additive Manufacturing Technology in Single β-Phase Field

Abdollah Saboori [1,*], Ata Abdi [2], Seyed Ali Fatemi [2], Giulio Marchese[1], Sara Biamino [1], Hamed Mirzadeh [2]

[1] Department of Applied Science and Technology, Politecnico Di Torino, Corso Duca degli Abruzzi 24, 10129 Torino, Italy

[2] School of Metallurgy and Materials Engineering, College of Engineering, University of Tehran, P.O. Box 11155-4563, Tehran, Iran

[*] Corresponding author: E-mail address: abdollah.saboori@polito.it, +39-011-0904763

Abstract

The hot working behaviour of additively manufactured Ti-6Al-4V pre-forms by Electron Beam Melting (EBM) has been studied at temperatures of 1000-1200 °C and strain rates of 0.001 to 1 s^{-1}. As a reference, a wrought Ti-6Al-4V alloy was also analyzed as same as the EBM one. In order to investigate the hot working behaviour of these samples, all the data evaluations were carried out step by step, and the stepwise procedure was discussed. No localized strain as a consequence of shear band formation was found in the samples after the hot compression. The flow stress curves of all the samples showed peak stress at low strains, followed by a regime of flow softening with a near-steady-state flow at large strains. Interestingly, it is found that the initial microstructure and porosity content as well as the chemistry of material (e.g. oxygen content) as being possible contributors to the lower level of flow stress that could be beneficial from the industrial point of view. The flow softening mechanism(s) were discussed in detail using the microstructure of the specimens before and after the hot deformation. Dynamic Recrystalization (DRX) could also explain the gentle oscillation in the appearance of the flow softening curves of the EBM samples. Moreover, the hot working analysis indicated that the activation energy for hot deformation of as-built EBM Ti-6Al-4V alloy was calculated as ~ 193.25 kJ/mol, which was much lower than the wrought alloy (229.34 kJ/mol). These findings can shed lights on a new integration of metal Additive Manufacturing (AM) and thermomechanical processing. It is very interesting to highlight that through this new integration, it would be possible to reduce the forging steps and save more energy and materials with respect to the conventional routes.

Keywords: Additive Manufacturing, Electron Beam Melting; Ti-6Al-4V alloy; Hot Compression; Softening mechanisms, Flow curve modelling

1. Introduction

Ti-6Al-4V alloy, which is an α + β titanium alloy, is a very well-known alloy in different sectors such as aerospace and biomedical. This considerable amount of application is mainly because of the low

1

density, high strength to weight ratio, excellent corrosion resistance, excellent fatigue performance, and biocompatibility of Ti alloys [1,2].

Forging is one of the main conventional processes that have been used in the production of Ti-6Al-4V parts [3]. In general, the production of titanium parts is divided in two steps; (I) production of titanium billets after the extraction via Kroll process and alloying, (II) shaping the billets via thermomechanical processes such as extrusion and forging [4]. However, this conventional production route of Ti-6Al-4V parts was found to be a low efficient and costly route. Therefore, over the last decades, several efforts, such as the substitution of electrode oxidation instead of the Kroll process, have been considered to reduce the production cost of Ti alloys [5]. In addition to the cost and efficiency of production, some inherent characteristics of titanium alloys such as their poor thermal conductivity and high reactivity to oxygen make their conventional production processing very challenging. Hence, powder-based manufacturing methods such as Additive Manufacturing (AM) processes have been explored as an important and effective solution. In fact, AM processes provide a more efficient and rather cheaper solution for the production of Ti parts and address all the challenges which have been reported in the production of Ti components [6,7].

Metal AM includes different technologies in which complex-shaped components are built in a layer-by-layer production process [1,8]. Nowadays, AM could attract lots of interests, mainly because of its flexibility in the production/repair of high-value components with a high grade of complexity that substantially needs more processing steps in conventional manufacturing/repairing routes [9,10]. As a matter of fact, in AM processes as advanced manufacturing technologies, a complex 3D near-net-shaped part can be produced in a single step and small lot sizes using metallic powder and a Computer-Aided Design (CAD) file [11,12].

Metal AM processes are classified in two main groups: Powder Bed Fusion (PBF) processes and Wire/Powder feed ones which are also known as Directed Energy Deposition (DED) processes [13,14]. In the PBF processes which are based on the melting of a powder bed selectively, two types of heat source can be employed: laser and electron beam. Indeed, the process using the laser is known as Laser Powder Bed Fusion (LPBF), and another one using the electron beam is defined as Electron Beam Melting (EBM) process [2,15–18]. The specific working conditions of the EBM process, such as the presence of a preheating step before the melting phase and high Vacuum chamber, make this process more promising with respect to other metal AM technologies, in particular for the production Ti parts [11]. These working conditions bring lots of advantages, such as negligible residual stress in the as-built state, high purity, high grade of powder recyclability and high productivity into this technology in comparison with other metal AM technologies [1,2,8,11,15].

Therefore, nowadays, metal AM technologies have been widely employed to produce Ti-6Al-4V parts [19,20]. However, despite overcoming all aforementioned challenges in the production of Ti-6Al-4V components, some other issues such as the presence of micro-voids and microstructural inhomogeneities are still present. Hence, Hot Isostatic Pressing (HIP) is introduced as a solution to eliminate not only the residual defects but also the columnar microstructure, which is formed during the building process. Nonetheless, it is very interesting to note that the mechanical properties of Ti pre-forms produced via EBM are rather comparable with those produced via conventional processes [21]. On the other hand, it is reported that through a well-controlled forging process that results in the

2

formation of a fine duplex microstructure including the primary α phase and Widmanstätten (α+β) regions, it would be possible the strengthen the alloy. This kind of microstructure is the most promising one to achieve the best properties, mainly owing to take the advantages of lamellar and globular microstructures. Thus, to achieve such a kind of microstructure, further thermomechanical processing is necessary.

In this regard, the combination of LPBF and thermomechanical processing has been recently considered as a promising approach to take the advantages of both processes [22–24]. It is found that higher performance levels can be achieved via the integration of AM into conventional manufacturing methods [25]. For instance, production of adapted pre-forms for the forging operations by AM technologies can result in the reduction of forging steps and consequently, material waste [26]. For this reason, the hot compression of LPBF Ti-6Al-4V alloy in the dual-phase α+β region (from 850 °C to 1000 °C) has been studied by Bambach et al. [4]. They found that the hot working performance and the resulted microstructure of AM and the wrought materials were similar. However, the LPBF one showed a lower level of flow stress and apparent activation energy of hot deformation. Nevertheless, according to the existing literature, the integration of EBM and thermomechanical processing as well as the hot working behaviour of as-built EBM Ti-6Al-4V alloy, in particular in the single-phase β-region, has not been considered and investigated. Hence, there is a lack of data on the microstructural evolution and deformation mechanism(s) in the hot deformation of EBM Ti-6Al-4V alloy in the single-phase β-region [27–30].

In addition, reports on the flow stress modelling of additively manufactured alloys are scant: FeCr alloy [31] and Ti-6Al-4V alloy [32]. Tao et al. [32] examined the suitability of the usual Arrhenius strain-compensation technique and Artificial Neural Network (ANN) model for prediction of flow stress of Ti-6Al-4V alloy during hot compression in the two-phase α+β region (from 700 °C to 900 °C). The widely used Arrhenius technique has so many parameters to be determined [33–37], and the ANN method does not give a simple flow stress formula for simulation purposes [38–40]. Therefore, a simple approach is required to model the flow stress, which also considers the pre-defined creep theories.

Therefore, this paper attempts to fill the knowledge gaps as regards the feasibility of the integration of the EBM process and thermomechanical processing as well as introducing a simple approach to model the flow stress of the EBM materials. For this reason, for the first time, hot deformation behaviour and microstructure evolution of EBM Ti-6Al-4V pre-forms were studied at temperatures of 1000-1200 °C and strain rates of 0.001 to 1 s^{-1}. All the finding for the EBM pre-forms were compared with those of wrought alloy. Moreover, the hot flow stress of EBM Ti-6Al-4V alloy was modelled and predicted via constitutive equations. All the constants of the constitutive equations and the activation energy of the hot deformation of this alloy produced by EBM process were calculated and reported.

2. Materials and Methods

2.1. Sample preparation

Extra-low interstitials (ELI) grade Arcam Ti-6Al-4V powder was employed as starting material to produce the cylindrical samples in this work. The chemical composition of the ELI Ti-6Al-4V powder

that is shown in Table 1 exhibits that the starting powder contains reduced levels of oxygen, nitrogen, carbon and iron. The starting powder used in this work has a particle diameter ranging from 45 to 106 μm and a volume median diameter of approximately 75 μm. Scanning Electron Microscopy (SEM) observation of powder revealed spherical particles, with homogeneous morphology, a rather smooth surface, few satellites around the particles and no internal porosity (Fig. 1(a-c)). An extruded rod with a diameter of 10 mm was considered as the wrought sample, where its chemical composition is also shown in Table 1.

Table 1: Chemical composition (wt.%) of the Arcam powder and wrought alloy used in this work.

Ti-6Al-4V	Al	V	C	Fe	O	N	H	Ti
Standard (ELI)	5.5-6.5	3.5-4.5	<0.08	<0.25	<0.13	0.05	<0.012	Bal.
Arcam (ELI)	6.41	3.86	0.02	0.19	0.09	0.01	0.002	Bal.
Wrought	6.2	4.1	0.01	0.2	0.12	0.01	0.001	Bal.

Ti-6Al-4V samples were built using an Arcam A2X EBM machine. The standard Arcam A2X build theme for Ti-6Al-4V (accelerating voltage of 60 kV, a layer thickness of 50 μm, and software version of 5.2.52) was used to produce the samples. All the cylindrical samples (Φ = 10 mm, h = 15 mm) for the hot compression test were built vertically, 5 mm above the start plate and connected to the start plate by means of standard thin wafer supports (Fig. 1(d)).
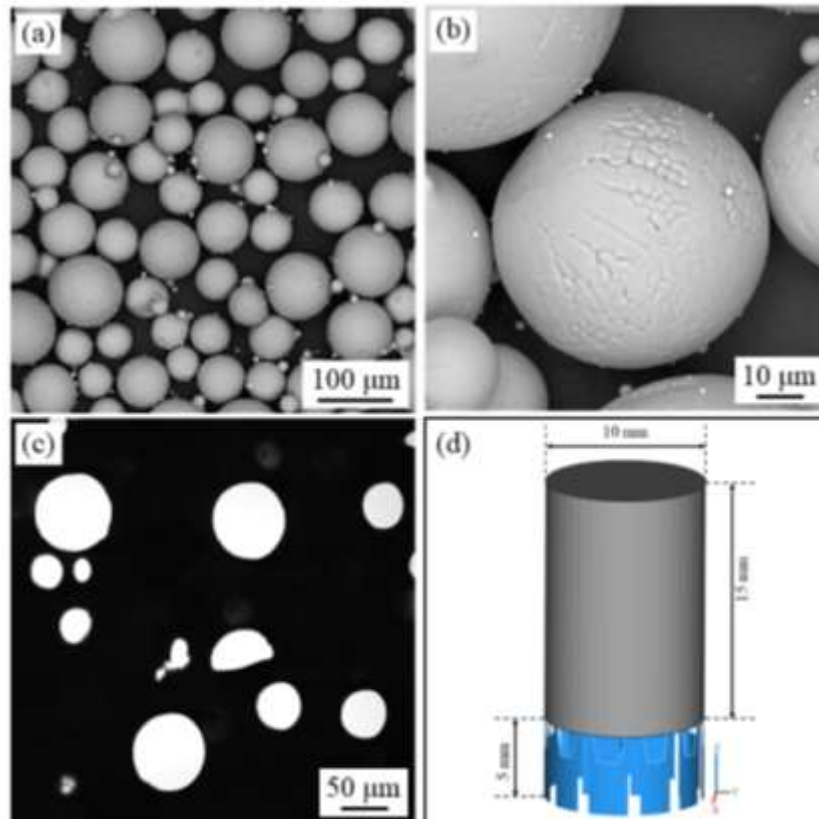

Figure 1. (a-b) SEM images, and (c) cross-section of starting Ti-6Al-4V powder, (d) design of the hot compression samples to be produced via EBM.

Prior to the powder spreading for the first layer, a stainless-steel start plate was preheated to 700 °C by electron beam scanning. After that, a layer powder was spread on the preheated start plate, and preheating phase of powder was started before its selective melting. This powder preheating before the fusion was repeated for each layer until the end of the building process. Throughout the EBM process, the entirety of the powder bed was kept at a temperature no lower than 580 °C. When the build is completed, the unmelted powder was blown off from the samples in a powder removal system (PRS) using the same powder and compressed air. Afterwards, all the wafer supports were removed from the samples by use of wire electrical discharge machining (WEDM) to prepare the samples for the hot compression tests.

2.2. Hot compression

The hot deformation tests were performed using a Zwick Roell Z250 universal machine equipped a load frame rate for a maximum load of 250 kN and a computer-controlled resistance furnace with a temperature accuracy of ± 5 °C. During the test, the load and displacement data were registered via a data acquisition system. The hot compression tests were carried out at temperatures in the range of 1000-1200 °C, which is the single-phase β region, with a step size of 50 °C, under strain rates of 0.001-1 s^{-1} up to the total strain of 0.70 (Fig. 2). Before the compression test, all the samples were kept for 5 min at the deformation temperature to achieve a uniform distribution of heat in the sample. In order to minimize the friction between the samples and anvils and consequently homogenize the compression force, a thin layer of mica was placed between the surfaces of the samples and the anvils. In this way, it would be possible to prevent the sticking issue during the quenching phase and facilitate a uniform deformation at high temperatures. After the hot compression test, to preserve the as-deformed microstructures, all samples were immediately water quenched.
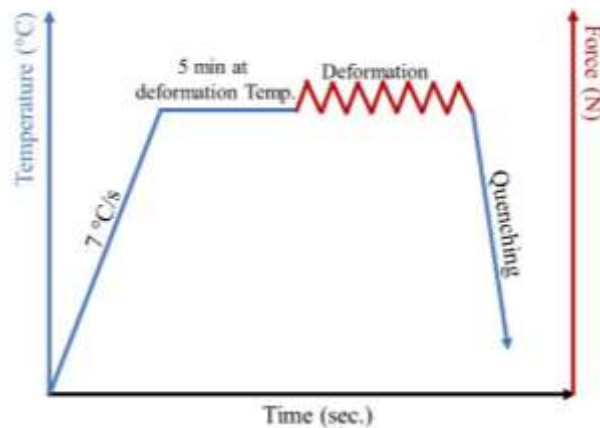

Figure 2. The heating and deformation cycle used in this work.

2.3. Characterization

Samples for microstructural analysis using optical and electron microscopes were cut parallel to the building and compression direction. Thereafter, their cross-sections were ground using 600 and 1000

grit SiC abrasive paper followed by 9 μm diamond paste. As the final surface preparation step, the as-polished surfaces were polished using a mixture of 1μm alumina particles and 10% of 30% H_2O_2. Finally, to accentuate the microstructure, the as-polished surfaces were etched employing Kroll's reagent (92 ml H_2O, 6 ml HNO_3 and 2 ml HF) [19,41]. The microstructures of as-built and as-deformed specimens were analyzed by a FEI Nova Field Emission Scanning Electron Microscopy (FESEM), a Leica Stereo and Optical Microscope (OM).

3. Results and discussion

3.1. As-built EBM and wrought microstructures

Microstructures of as-built EBM and wrought samples are shown in Fig. 3 and Fig. 4. As previously reported by several researchers [2,20], and can be seen in Fig. 3, as-built EBM samples characterized by long columnar β grains along the building direction (Fig. 3(a)) as well as lamellar structure with fine α platelets oriented in different directions. This type of oriented fine α platelets is also known as Widmanstätten microstructure (Fig. 3(b)). FESEM image in Fig. 3(b-c) clearly shows that despite the presence of some α colonies (parallel α platelets), most of the α platelets are individual that can be a direct consequence of a rather high cooling rate during the transformation of β→α. Besides, a continuous α layer was found along the prior β grains that is called as α_{GB}. This epitaxial growth of the β grains that leads to the formation of columnar grains in the direction of the maximum thermal gradient (namely is the building direction) can result in a high grade of anisotropy in the material.
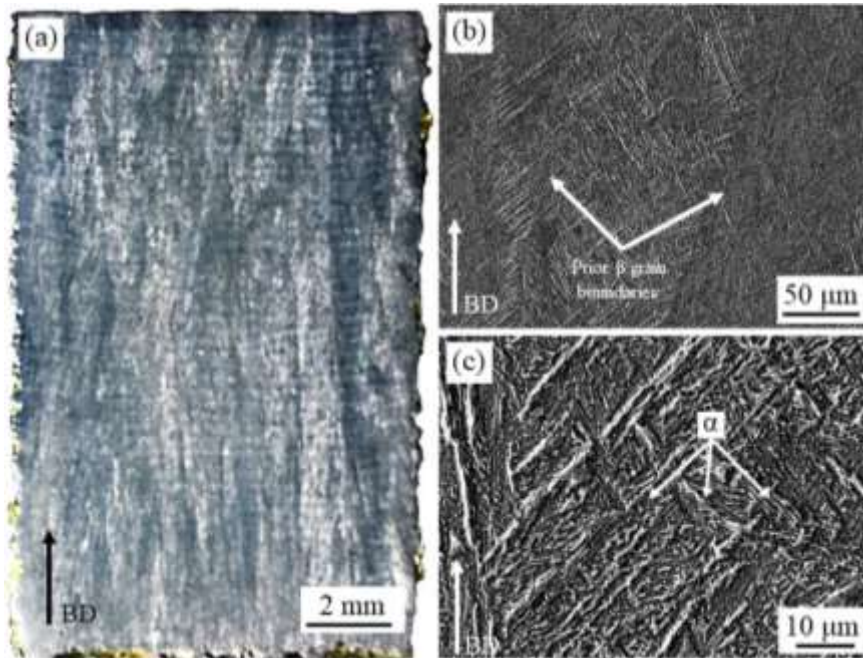

Figure 3. (a) Stereomicrograph of the as-built EBM Ti-6Al-4V sample, (b-c) SEM image of as-built EBM Ti-6Al-4V sample at two different magnifications.

As a reference alloy, a wrought α + β titanium alloy (Ti-6Al-4V), was also considered and investigated. As same as the EBM one Fig. 4 shows the bimodal or duplex α + β microstructure of the as-received

wrought Ti-6Al-4V alloy. The average grain size, which was evaluated by the intercept method, is 53 ± 5 μm (Fig. 4(b)). As can be seen in Fig. 4(c), the wrought alloy primarily includes equilibrium α and β phases which are shown by arrows (phase β is the white phase, and phase α is the black one).
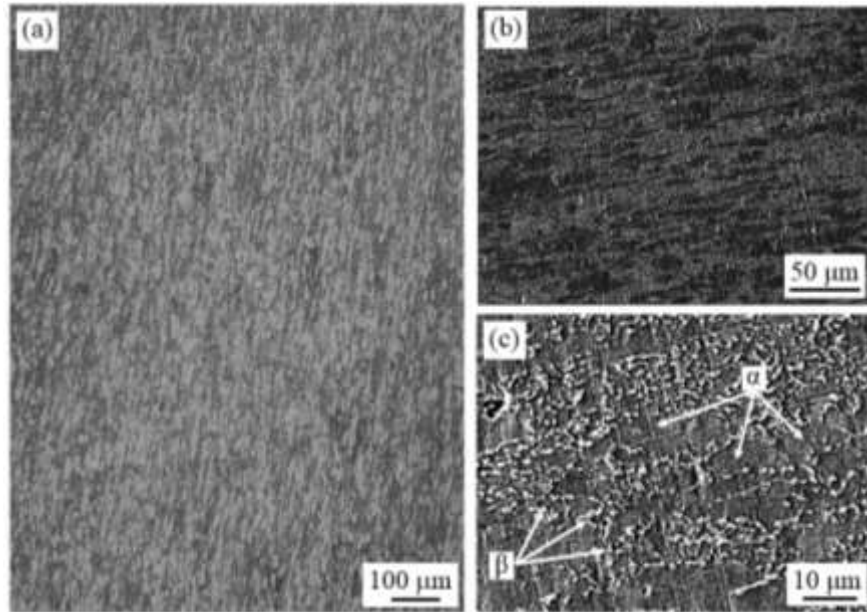

Figure 4. (a) Stereomicrograph of the as-received wrought Ti-6Al-4V sample, (b-c) SEM image of as-received wrought Ti-6Al-4V sample at two different magnifications.

The porosity content of both specimens in the as-received state was evaluated through the image analysis method. It is revealed that the porosity content of the as-built EBM cylinders (0.13 ± 0.05%) are slightly higher than those of wrought alloy (0.061 ± 0.002%). Since the response of each material against any external load is directly corresponds to its microstructure [42–44], different flow softening behaviours in two different materials (as-EBM and wrought) can be expected.

3.2. Flow softening behaviour

Fig. 5(a) demonstrates examples of the hot compression flow curves of the EBM and wrought Ti-6Al-4V alloy deformed in the temperature range of 1000-1200 °C and strain rates range of 0.001 to 1 s^{-1}. These graphs were plotted using the true stressed which are determined via the division of load over the surface area. The true strains also calculated through the equation of $\varepsilon = -ln(l/l_0)$ in which l_0 is the starting height, and l is the instantaneous height of the samples. As can be seen in this figure, all the samples show somewhat similar flow softening behaviour in which the stresses reach a peak at a critical strain and then remain in rather steady-state stresses. However, it should be noticed that the difference in their specific stress behaviour can be related to the initial chemical composition, microstructure, temperature and strain rate [45]. Fig. 5(b) exhibits the flow curves of the samples after the hot deformation at different temperatures and a constant strain rate of 0.1 s^{-1}. This Figure clearly shows that by increasing the deformation temperature, the flow stress decreases. In addition, as can be seen in Fig. 5(a-b) by increasing the deformation temperature and decreasing the strain rate the difference

between the flow stress of the EBM and wrought samples decreases that can be as a result of higher diffusion rate at higher temperatures.

It is very interesting to highlight that in Fig. 5(a-b) also reveal that at each deformation condition, the flow stress of EBM alloy is lower than that of wrought one. This difference can be related to the effect of initial microstructure, defect and oxygen contents of the starting materials. In fact, it is revealed that while the oxygen content of the EBM samples was lower (Table 1) than the wrought material, their porosity content was slightly higher than those of wrought. However, it should be noticed that in both cases no porosity was found after the hot deformation process. This easier flow softening behaviour of the EBM samples can be considered as a benefit for the pre-forms produced via this technology in comparison with that of wrought.
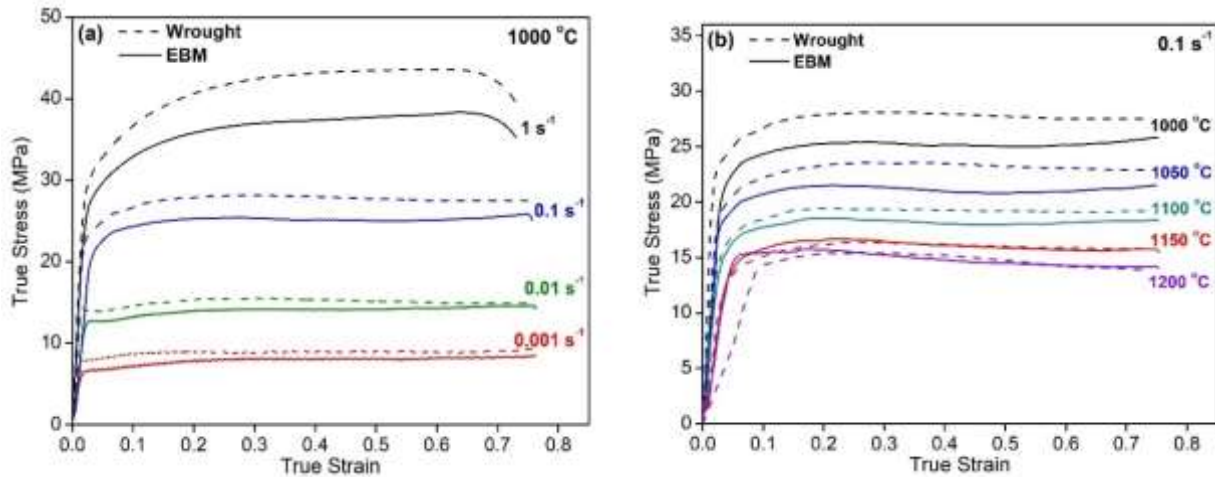

Figure 5. True stress-strain curves of as-built EBM and wrought Ti-6Al-4V alloy indicating the effect of (a) strain rate, and (b) compression temperature.

In general, the appearance of the flow softening curves provides some information that facilitate the recognition of the mechanism of hot deformation. It is found that at strain rates lower than 0.1 s^{-1} the curves were of almost steady-state type at all the temperature range. This type of flow softening curves implies that the mechanisms of softening were as fast as the work hardening rate. This flow softening behaviour can be an indication of different mechanisms such as Dynamic Recrystallization (DRX), Dynamic Recovery (DRV) or superplasticity that could happen at very high rates [27]. Sheppard et al. reported that DRV could be considered as the primary dynamic restoration mechanism in the β phase mainly because of its crystallographic structure which is Body-Centered Cubic (BCC) and the high Stacking Fault Energy (SFE) of the material [23,46]. On the other hand, as can be seen in Fig. 5, in the stress-strain curves, in particular at high temperatures and low strain rates there are some oscillations that can be considered as an indication of DRX.

In general, when DRV occurs, the flow softening curves have a simple shape in which at low strains strain hardening takes places that continuo to reach a steady-state flow at high strains. In materials with high SFE, like Ti-6Al-4V, the generated dislocations during the deformation at the beginning become entangled and thereafter climb and annihilation would occur that leads to the formation sub-grains in the grain interiors. On the other hand, Seshacharyulu et al. reported that in the Ti-6Al-4V alloy, in the

8

β phase regime, DRX is the dominant restoration mechanism [27]. Hence, further investigations such as microstructural analysis are necessary to define the hot deformation mechanism (s).

Typical microscopic images of Ti-6Al-4V EBM specimens after the hot deformation in the single β region are shown in Fig. 6. Interestingly, it is found that after the hot compression, no indication of localized shear band formation was revealed in all the samples. As it can be seen barreling, which is a well-known phenomenon in the open-die forging occurred in the samples after the hot compression (Fig. 6(a)). As can be seen, each sample consists of three distinct zones; "dead" zone at the top and bottom of the specimens which was in contact with the anvils, "severe plastic deformation" zone in the center and "partially plastic deformation" zones in the lateral sides of the specimens.
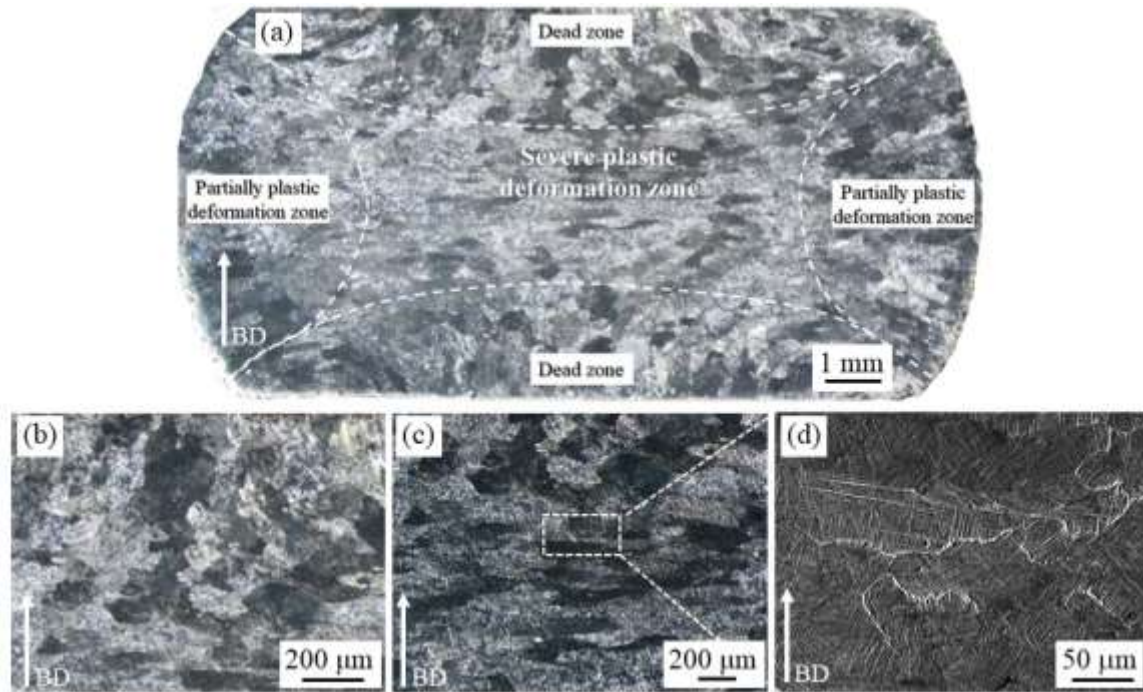

Figure 6. (a)Typical macro-image of EBM Ti-6Al-4V samples deformed at 1000 °C/0.1 s^{-1}, (b) optical micrograph of the dead zone, (c) optical micrograph of the severe plastically deformed zone, (d) FESEM micrograph of (c) at higher magnification.

A representative microstructure of the dead zone, which is shown in Fig. 6(b) shows that no restoration mechanism(s) was activated during the hot compression. Thus, no significant microstructure change was found in these zones. This behaviour is mainly owing to the effect of heat exchange and friction with the anvils. Whereas, in the severe plastic deformation zone which is shown in Fig. 6(c-d) it is clear that even if the deformation features are destroyed because of cooling across the transus temperature, some signs of DRX such as irregular prior β grain boundaries is detectable. In addition, it is revealed that the grain after the hot compression become rather elongated in the direction perpendicular to the applied force. The presence of these elongated grains can be attributed to the work-hardening accompanied by DRV mechanism during high-temperature deformation. Therefore, for the microstructural analysis to define the hot deformation mechanism, all the attention was paid in the inner sever plastic deformation zone. Microstructural analysis shows that the starting structure, hot

working condition and subsequent cooling rate after the hot compression, are the key factors that define the microstructure evolution. Fig. 7 exhibits the microstructure of the EBM and Wrought Ti-6Al-4V alloys from the severe plastic deformation zone after the hot compression at 1000 °C and strain rate of 0.1 s^{-1}. This figure clearly shows that curved grain boundaries surround the dynamically recrystallized grains [47,48]. In fact, the recrystallized grains are relatively fine compare to the original grains and their nucleation initially started from the prior beta grains and then next to the recrystallized grains. However, it should be note that the quenching of specimens after the hot compression that resulted in the phase transformation of β→α' made the detection of DRX grains very challenging [48]. Therefore, this figure which suggests the incident of DRX, can also explain the gentle oscillation in the appearance of the flow softening curve, in particular at higher temperatures and lower strain rates [49,50]. These findings suggest that when hot deformation is performed at the temperatures above the tarnsus temperature, the flow softening curves are almost constant, which indicate that DRV and DRX were in operation. Nonetheless, the degree of DRX can be varied with the initial microstructure, strain rate and temperature [51]. In addition, it is very interesting to noted that in the as-deformed EBM samples in comparison with the as-built state that characterized by columnar grains with the average grain width of 95.4 ± 9.7 µm and grain length up to several millimeters, the grains are much finer.
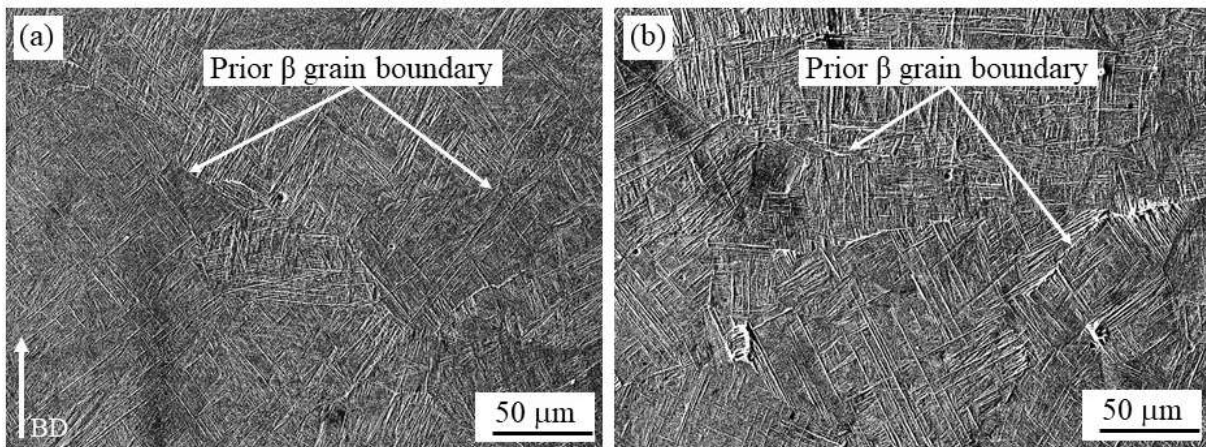

Figure 7. FESEM micrograph of the cross-section of (a) EBM, (b) Wrought Ti-6Al-4V alloy after the hot compression at 1000 °C and strain rate of 0.1 s^{-1}.

Fig. 8 compares the initial and deformed microstructures of EBM and wrought Ti-6Al-4V samples after the hot compression at 1000 °C and strain rate of 0.1 s^{-1}. As can be seen, when hot deformation is carried out in the single β regime which is above the transus temperature, almost all the prior α phases may be transformed into the high temperature β phase. This phase transformation can happen before the hot compression or when the sample is under the hot compression. In general, it is reported that in the most of metallic alloys the driving force which is necessary for recrystallization comes from the stored energy as a consequence of the dislocation density. This stored energy is found to be in the range of 10-100 J/mol [51]. Whereas, the stored energy for solid-phase transformation arises from the diversity of the free energies between the constituent phases. This driving force was found to be about 1.0 kJ/mol [51,52]. This significant difference between these two required stored energies for recrystallization and phase transformation suggests that, during the hot compression test, occurrence

of phase transformation needs more stored energy in comparison with DRX [51]. Therefore, in the case of EBM sample with finer α lath thickness since the kinetics of phase transformation is faster, the required driving force for DRX during the hot compression is provided and thus the oscillations as a result of DRX in the EBM curves are more visible with respect to the wrought one. This finding can also confirm that the degree of DRX in the EBM samples can be higher than the wrought alloy. The microstructure of quenched samples suggests that this β phase is likely transformed into fully acicular martensite after the hot compression. It is important to highlight that in the case of EBM Ti-6Al-4V, it would be possible to achieve a higher degree of phase transformation (α→β) during the holding step before the hot compression test (insets in Fig. 9(a-b)). This discrepancy can be related to the size of α phases in the EBM samples which are finer than those in the wrought alloy. In fact, α thickness evaluations via image analysis exhibited that this value for the EBM and wrought alloys were 1.45±0.52 μm and 3.54±0.75 μm, respectively. This difference in the size of α phases can change the kinetics of transformation and leads to a higher transformation in the case of EBM samples [53]. On the other hand, the as-built EBM samples that, on the contrary of the wrought alloy, is produced via a rapid solidification process may have higher quantity of the beta phase [54]. This difference in the degree of the phase transformation as well as different phase fractions in both samples can result in a higher β content with the BCC structure during the hot compression of the EBM samples [55]. Therefore, the difference in the thickness of α platelets and phase fractions together with the higher porosity content as well as the lower oxygen content can be considered as the possible reasons for having lower flow stresses in the case of EBM samples.
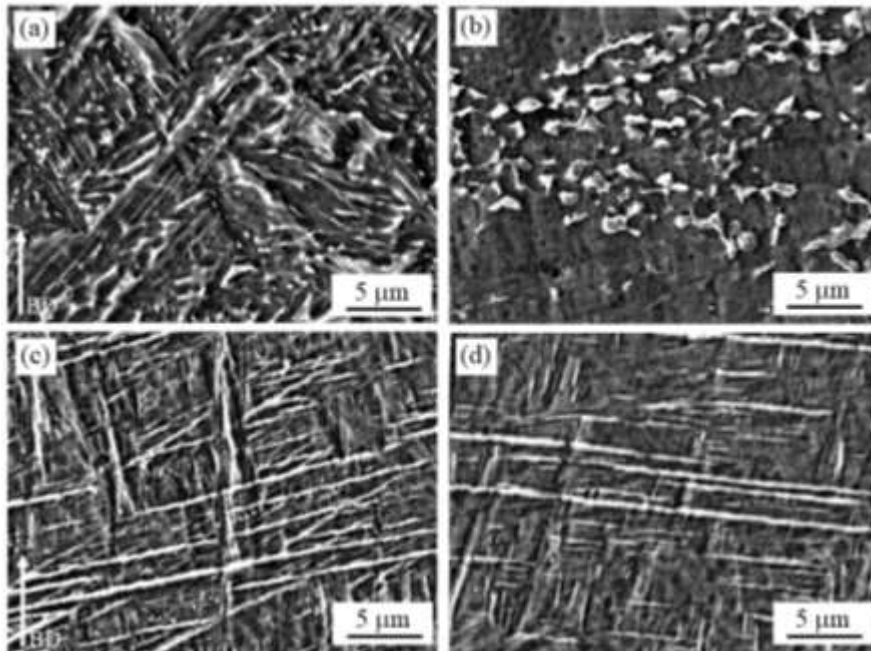

Figure 8. FESEM micrograph of (a) as-built EBM, (b) as-received wrought, (c) as-deformed EBM and (d) as-deformed wrought Ti-6Al-4V alloy hot compressed at 1000 °C and strain rate of 0.1 s^{-1}.

Fig. 9 compares the general microstructure of the EBM and wrought Ti-6Al-4V alloy in the as-homogenized state. As can be seen the EBM sample characterized with a coarser grain that could be

as a consequence of the nature of AM process. As a result, this coarser grain reduces the resistance to dislocation sliding and facilitate the dynamic softening mechanism to take place during the hot compression [51].
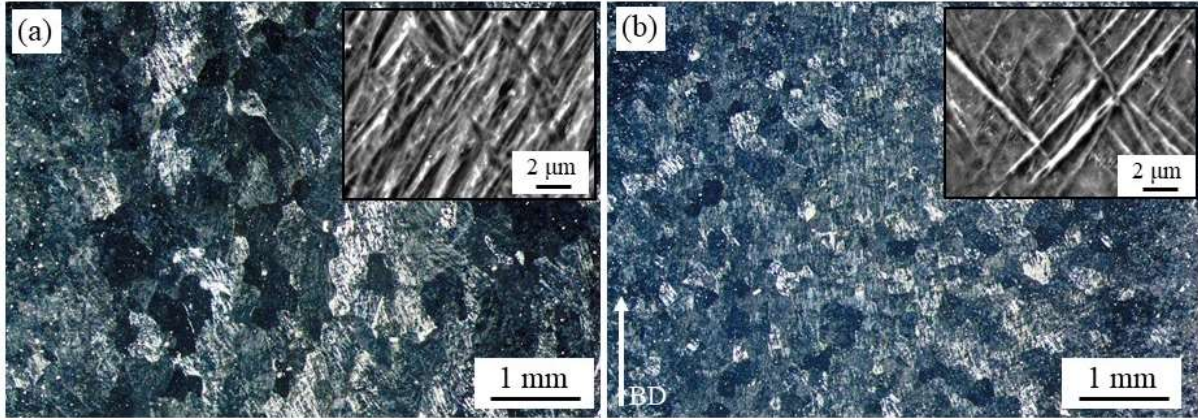

Figure 9. OM microstructure of (a) EBM, (b) wrought Ti-6Al-4V samples after homogenization for 5 min at 1000 °C.

3.3. Constitutive analysis

In general, the flow stress of the metallic materials during thermomechanical processing can be determined by using constitutive equations based on the fundamental one that is given as follow:

$$Z = \dot{\varepsilon} exp\left(\frac{Q}{RT}\right) = f(\sigma) \tag{1}$$

Where Z is the Zener-Hollomon parameter that is also considered as the temperature compensated strain rate, and Q is the deformation activation energy. By consideration of the Zener-Hollomon parameter (Eq. 1), the power-law creep equation (Eq. 2) can be rewritten as Eq. 3 [56]:

$$\dot{\varepsilon} = Aexp(-\frac{Q}{RT})\sigma^n \tag{2}$$

$$Z = \dot{\varepsilon} exp\left(\frac{Q}{RT}\right) = A\sigma^n \tag{3}$$

where n is the stress exponent and A is a constant. Taking natural logarithm from both sides of Eq. 3 results in the following expression:

$$ln\dot{\varepsilon} = \left[lnA - \frac{Q}{RT}\right] + n\, ln\sigma \tag{4}$$

According to this equation, n can be calculated based on the slope of the plot of $ln\dot{\varepsilon} - ln\sigma$. Since in the calculation of n and Q using this equation, no specific strain is recommended, the flow stresses related to either steady-state or peak can be utilized [57,58]. Hence, for these calculations, the stresses associated with the strain of 0.5 are considered from the flow stress curves. The estimated stress exponent n for this alloy in the single β region is ~ 4.37, 4.25, and 4.32 for the EBM material deformed

at 1000 °C, the EBM material deformed at 1100 °C, and the wrought material deformed at 1000 °C, respectively (Fig. 10(a)).
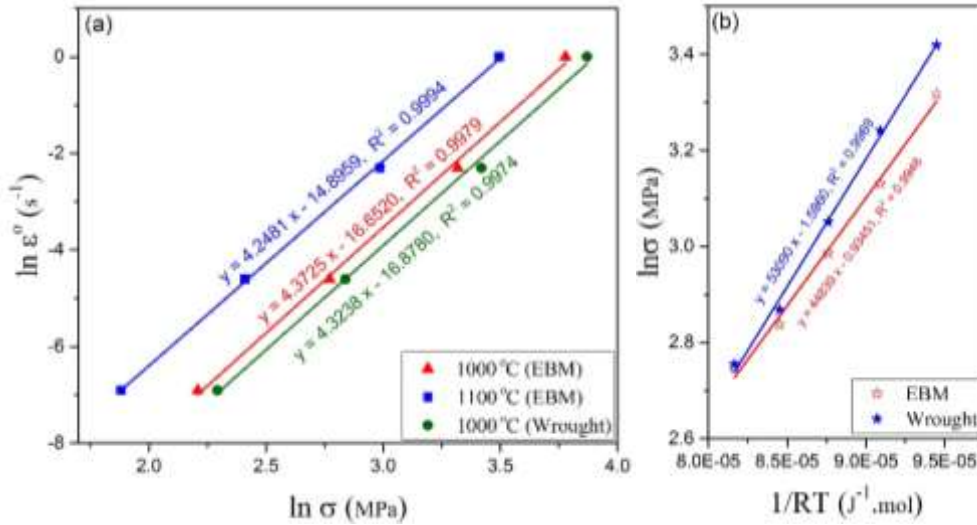

Figure 10. Plots used to obtain (a) *n* and (b) *Q* for hot deformed materials.

These values are well comparable with a value of 4.3, which has been reported for a superplastic Ti-6Al-4V alloy [51]. On the other hand, these values are very close to the theoretical value of 4.5 which is related to the deformation mechanism of glide and climb of dislocations in the climb-controlled regime [59,60] as a usual hot deformation mechanism of Ti-6Al-4V alloy [61–63]. After that, based on the confirmed deformation mechanism, the *n* values of 4.31 and 4.32 were used in this section to calculate the activation energy of deformation for the EBM and wrought Ti-6Al-4V samples, respectively. This consideration makes the analysis more reliable for both samples (EBM and wrought).

Substantially, activation of deformation can be calculated from a partial differentiation of Eq. 4 that results in the following equation:

$$ln\sigma = \left\{\left(\frac{1}{n}\right)(ln\dot{\varepsilon} - lnA)\right\} + \left(\frac{Q}{n}\right)\left(\frac{1}{RT}\right) \qquad (5)$$

According to Eq. 5, as shown in Fig. 10(b), the slope of the plot of $ln\sigma - 1/RT$ gives the value of Q/n. As a result, by consideration of $n_{EBM} = 4.31$ *and* $n_{wrought}=4.32$, the activation energy of deformation for the EBM and wrought samples are about ~ 193.25 kJ/mol and 229.34 kJ/mol, respectively. Interestingly, it can be seen that the Q value in EBM material is lower than the wrought material. This finding is entirely in agreement with the microstructural evaluations. As mentioned earlier, in the EBM samples which have coarser β grains, the dislocations can slide easier and consequently results in lower activation energy of deformation. Moreover, both deformation activation energies are lower than that of reported for the hot deformation in the α+β region (668 kJ/mol) [4]. This considerable difference is the direct consequence of the phase composition of the material before and after the transus temperature. In fact, in the single β phase region the existence of almost full BCC β phase with more slip system and higher diffusion coefficient compared to the HCP α phase, can increase the feasibility

of the deformation and reduce the activation energy. These findings are in line with those reported by Seshacharyulu et al. [49] and in contrast with Ding et al. [51]. This contradiction in the values of the deformation activation energy can consolidate the idea that the activation energy depends strongly on microstructure and chemical composition of materials. On the other hand, what is interesting about the value of the activation energy of deformation is that in both cases they are very close to that for lattice self-diffusion activation energy of titanium in the β region (251.2 kJ/mol) [64,65]. It should be noted that for the deformation mechanism of glide and climb of dislocations, the deformation activation energy is the lattice self-diffusion one [59,60].

As mentioned earlier, the Zener-Hollomon parameter, which also known as temperature compensated strain rate, is extensively employed in the hot deformation studies. Therefore, to explore the correct relationship between Z and σ, Eq. 3 was used. For this reason, at first, the natural logarithm of Eq. 3, which can be expressed as follow is used to calculate the final n values by consideration of all data for each material.

$$lnZ = lnA + n\, ln\sigma \tag{6}$$

According to this equation, the slope of the plot of $ln\,Z$-$ln\,\sigma$ can be considered as the final value of n (Fig. 11(a)). Therefore, according to the plots, the values of n were determined as 4.36 and 4.35 for EBM and wrought materials, respectively. After that, by using these values, it would be possible to determine the correlation between Z and σ as follows:

$$Z^{1/4.36} = A^{1/4.36}\sigma \iff EBM \tag{7}$$

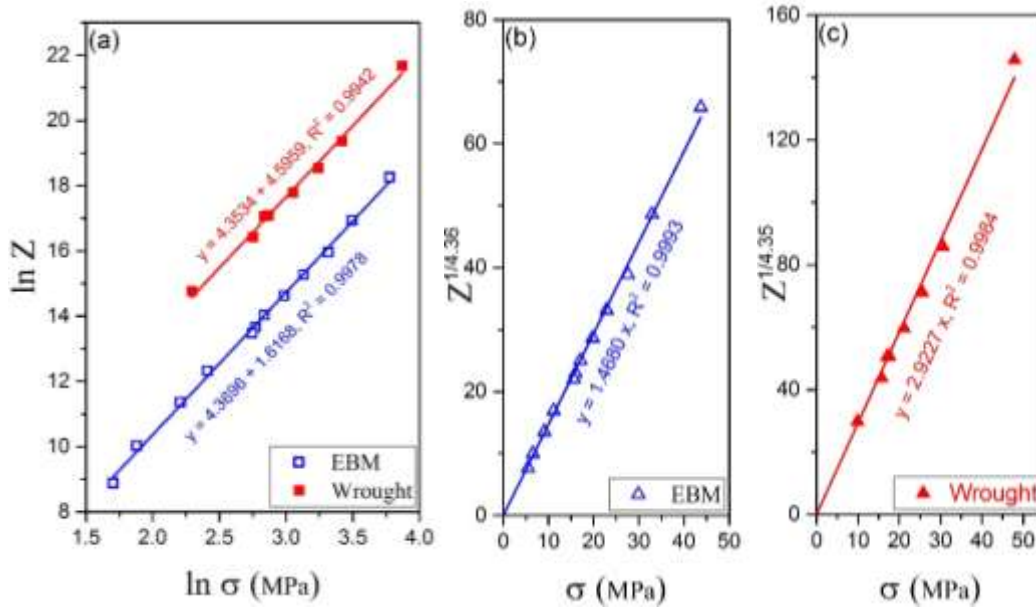$$Z^{1/4.35} = A^{1/4.35}\sigma \iff Wrought \tag{8}$$

Figure 11. Plots used for obtaining (a) the final value of n and (b) A for hot deformed EBM sample, (c) A for hot deformed wrought sample.

Accordingly, as shown in Fig. 11(b) and Fig. 11(c), the slope of the plot of $Z^{1/4.36} - \sigma$ and $Z^{1/4.35} - \sigma$ with the intercept of zero gives the value of $A^{1/4.36}$ and $A^{1/4.35}$, respectively. As a result, the value of A was determined as ~ 5.33 and 106.209 for EBM and wrought materials, respectively. Therefore, the following equations can be proposed to express the flow stress at a strain of 0.5 during hot deformation of these materials:

$$Z = \begin{cases} \dot{\varepsilon} \exp\left(\frac{193250}{RT}\right) = 5.33\sigma^{4.36} \iff EBM \\ \dot{\varepsilon} \exp\left(\frac{229340}{RT}\right) = 106.209\sigma^{4.35} \iff Wrought \end{cases} \tag{8}$$

the calculated flow stress values of the EBM material at a strain of 0.5 are plotted against the experimental values of flow stress in Fig. 12. As can be seen in this graph, there is an excellent agreement between the calculated flow stress and the experimental values.

However, the ability of the model can be better evaluated by calculating the root mean square error (RMSE) and the percentage of the average relative absolute error (AAE) using the following formulae:

$$RMSE = \sqrt{\frac{1}{N}\sum_{i=1}^{N}(t_i - y_i)^2} \tag{9}$$

$$AAE = \frac{1}{N}\sum_{i=1}^{N}\left|\frac{t_i - y_i}{t_i}\right| \times 100 \tag{10}$$

where t_i is the target output, y_i is the model output, and N is the number of data points. The average RMSE and AAE were determined as 0.54 MPa and 2.46%, for EBM sample and 0.81 MPa and 2.23% for the wrought samples, respectively. These low error values confirm the suitability of the developed constitutive equation for modelling and prediction of flow stress.
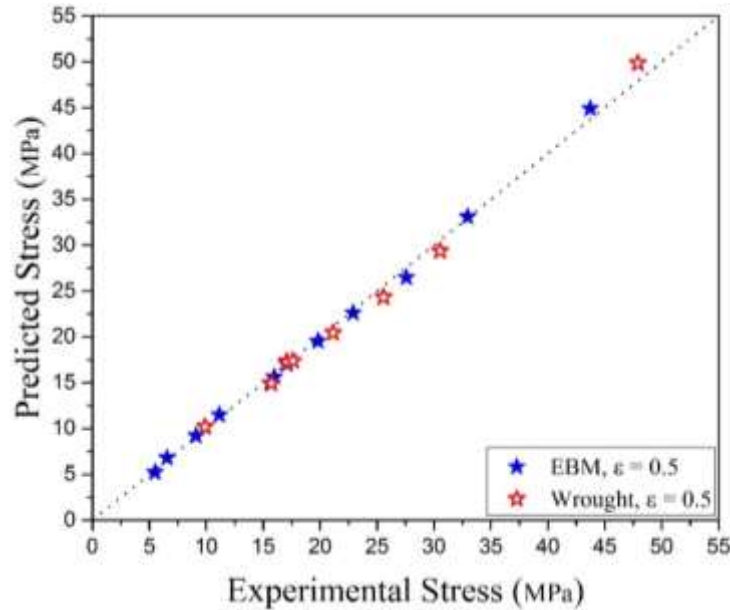

Figure 12. Calculated flow stress values at a strain of 0.5 versus the experimental values.

15

3.4. Flow stress modelling

Based on the analyses of Section 3.3, for the EBM and wrought samples, the Q values of 193.25 kJ/mol and 229.34 kJ/mol and n values of 4.36 and 4.35 were achieved, respectively. By using these values, it would be possible to define the dominant deformation mechanism of both materials during hot working, which is consistent with the deformation mechanism of glide and climb of dislocations in the climb-controlled regime. Moreover, it was shown that the value of A in Eq. 3 is different for these materials, where the obtained values of A were determined for the strain of 0.5. Therefore, the abovementioned analyses can be used at other strains to find the dependency of A on the strain. Accordingly, for each strain (0.05 to 0.65), the slope of the plots of $Z^{1/4.36} - \sigma$ and $Z^{1/4.35} - \sigma$ with the intercept of zero was used to obtain the value of $A^{1/4.35}$ and $A^{1/4.36}$ for EBM and wrought materials, respectively. The results are shown in Fig. 13(a) and Fig. 13(b) for strains of 0.2 and 0.65, apiece. Finally, the calculated values of A are summarized in Fig. 13(c), where a mathematical function has been fitted on the data to show the dependence of A on the strain. In this way, it is possible to model the flow curves. For this purpose, the following equations can be introduced:

$$Z = \begin{cases} \dot{\varepsilon} \exp\left(\frac{193250}{RT}\right) = 3.81147 \times \exp\left(0.16762/(\varepsilon + 0.07671)\right) \times \sigma^{4.36} \Leftrightarrow EBM \\ \dot{\varepsilon} \exp\left(\frac{229340}{RT}\right) = 85.30065 \times \exp\left(0.11007/(\varepsilon + 0.03775)\right) \times \sigma^{4.35} \Leftrightarrow Wrought \end{cases} \tag{11}$$
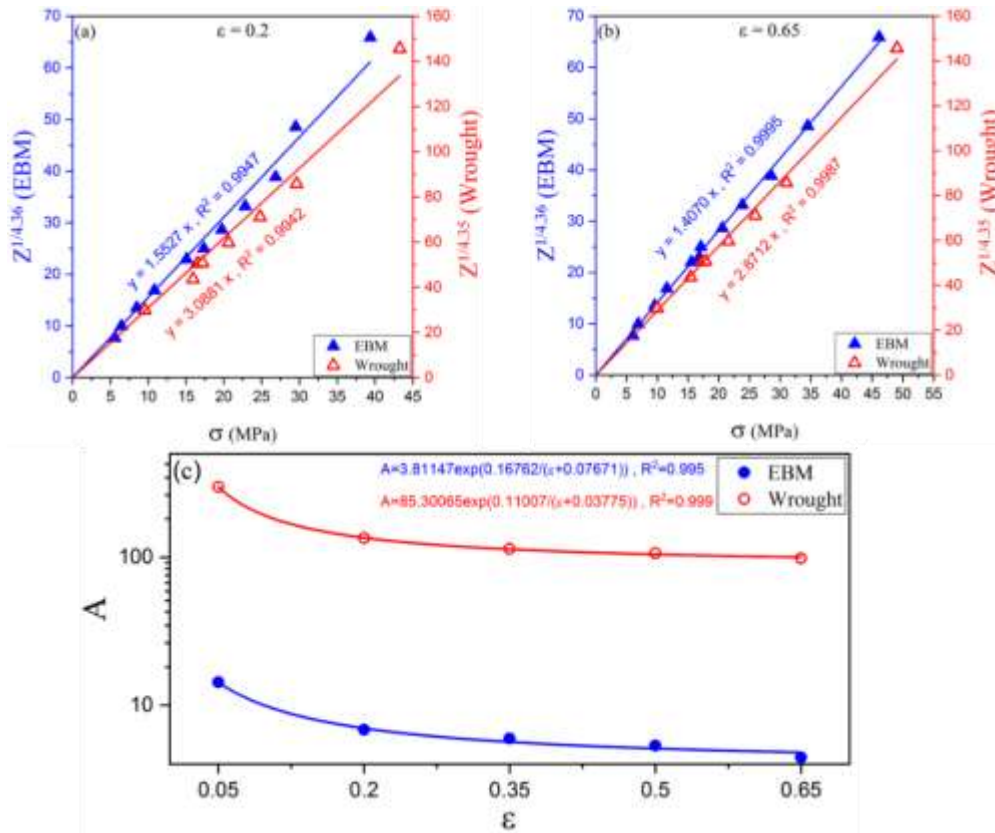

Figure 13. Plots used for obtaining A for hot deformed materials at the strain of (a) 0.2 and (b) 0.65. Part (c) represents the calculated values of A versus strain for both materials.

16

Fig. 13 (c), clearly demonstrate that in all the strains, the *A* value for the EBM sample is markedly lower than that of wrought one. According to Sheppard et al. *A* parameter can be interpreted as a measurement index of the frequency with which dislocations might prevail over barriers [46]. In addition to the microstructural observation and flow softening curves, these lower values of *A* parameter for the EBM samples also confirm that over the wide range of strains (up to 0.65) EBM pre-forms can be deformed easier in comparison with the wrought one. This compelling advantage of EBM material compared to the wrought material leads to a reduction in the tool load and easier hot deformation.

For the EBM material, Eq. 11 was used to model the flow stress, where the average RMSE was obtained as 2.42 MPa, which reveals the suitability of the proposed equation for modelling and prediction of hot deformation flow stress. Fig. 14 presents some calculated hot deformation flow stresses as compared to the experimental ones. It can be seen that the modelling ability of this technique with consideration of experimental *n* and *Q* values is outstanding.
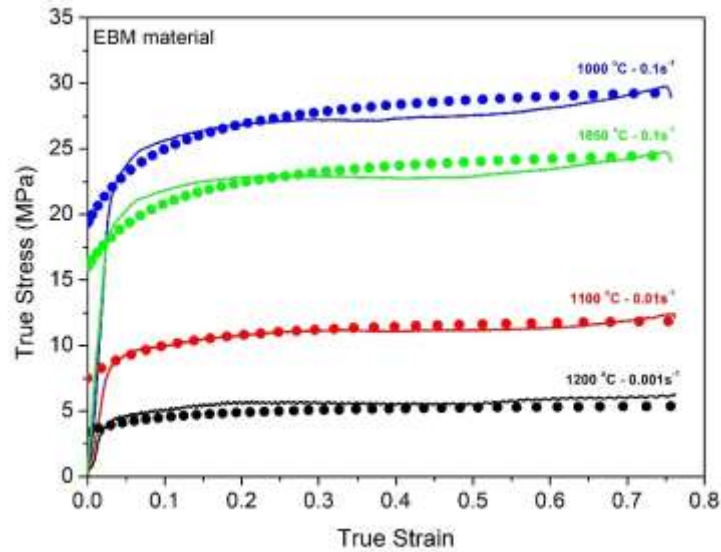

Figure 14. Comparison of the experimental (solid lines) and predicted (dotted lines) flow curves.

4. Conclusions

This work shed lights on a novel integration of metal Additive Manufacturing of pre-forms and thermomechanical processing. The flow softening behaviour and microstructure evolution of AM pre-forms were investigated and compared to the wrought material as a conventional material. The outcomes are analyzed using the available materials models, and the following conclusions can be drawn as follow:

- While, the as-built EBM sample exhibited long columnar β grains along the building direction as well as lamellar structure with fine α platelets oriented in different directions, the wrought material showed an equiaxed α-β microstructure with slightly elongated grains.

17

- All the samples show somewhat similar flow softening behaviour in which the stresses reach a peak at a critical strain and then remain in rather steady-state stress. However, at each deformation condition, the flow stress of EBM alloy is lower than that of wrought alloy, which can be related to the effect of initial microstructure, such as the thickness of α platelets and grain size, slightly higher defect and lower oxygen contents in the EBM sample.
- After the deformation of all the samples, no indication of localized shear band formation was revealed.
- After the hot compression, the porosity content of the EBM pre-forms was reduced significantly in such a way that no porosity was found in the EBM samples after the deformation.
- After the hot deformation in the single β zone, the trend of the flow softening curves are almost constant, which indicate that DRV and DRX were in operation. Nonetheless, the degree of DRX can be varied with the strain rate and temperature.
- Even if the deformation features are destroyed because of cooling across the transus temperature, some signs of DRX such as irregular prior β grain boundaries was detectable. This observation confirms the occurrence of DRX can also explain the gentle oscillation in the appearance of the flow softening curve, in particular at higher temperatures and lower strain rates.
- This difference in the degree of the phase transformation as a consequence of various thickness of α platelets results in a higher β content with the BCC structure during the hot compression of the EBM samples.
- Over the wide range of strains (up to 0.65), the A value is markedly lower for the EBM sample that confirms the higher deformability of the EBM pre-forms in comparison with the wrought one.
- The activation energy of deformation for the EBM and wrought samples are about ~ 193.25 kJ/mol and 229.34 kJ/mol, respectively. Interestingly, the Q value in EBM material is lower than the wrought material. However, in both cases, the activation energy of deformations is very close to that for lattice self-diffusion activation energy of titanium in the β region (251.2 kJ/mol).
- The average RMSE and AAE were determined as 0.54 MPa and 2.46%, for EBM sample and 0.81 MPa and 2.23% for the wrought samples, respectively. These low error values confirm the suitability of the developed constitutive equation for modelling and prediction of flow stresses.

Data availability

The authors stated that the processed data required to reproduce these findings were available in this manuscript.

Funding

References

[1]   M. Liu, S. Liu, W. Chen, C. Chen, Y. Lv, X. Zhang, P. Lei, Y. Lin, K. Zhou, Effect of trace lanthanum hexaboride on the phase, grain structure, and texture of electron beam melted Ti-6Al-4V, Addit. Manuf. 30 (2019) 100873. doi:https://doi.org/10.1016/j.addma.2019.100873.

[2]   S. Liu, Y.C. Shin, Additive manufacturing of Ti6Al4V alloy: A review, Mater. Des. 164 (2019) 107552. doi:https://doi.org/10.1016/j.matdes.2018.107552.

[3]   B. Dutta, F.H.S. Froes, The Additive Manufacturing (AM) of titanium alloys, Met. Powder Rep. (2017) 1–11. doi:10.1016/j.mprp.2016.12.062.

[4]   M. Bambach, I. Sizova, A. Emdadi, Development of a processing route for Ti-6Al-4V forgings based on preforms made by selective laser melting, J. Manuf. Process. 37 (2019) 150–158. doi:https://doi.org/10.1016/j.jmapro.2018.11.011.

[5]   I. Mellor, L. Grainger, K. Rao, J. Deane, M. Conti, G. Doughty, D. Vaughan, 4 - Titanium powder production via the Metalysis process, in: M. Qian, F.H. [(Sam) Froes] (Eds.), Titan. Powder Metall., Butterworth-Heinemann, Boston, 2015: pp. 51–67. doi:https://doi.org/10.1016/B978-0-12-800054-0.00004-6.

[6]   F.H.S. Froes, M.N. Gungor, M. Ashraf Imam, Cost-affordable titanium: The component fabrication perspective, JOM. 59 (2007) 28–31. doi:10.1007/s11837-007-0074-8.

[7]   G. Del Guercio, M. Galati, A. Saboori, Innovative Approach to Evaluate the Mechanical Performance of Ti--6Al--4V Lattice Structures Produced by Electron Beam Melting Process, Met. Mater. Int. (2020).

[8]   S. Biamino, A. Penna, U. Ackelid, S. Sabbadini, O. Tassa, P. Fino, M. Pavese, P. Gennaro, C. Badini, Electron beam melting of Ti–48Al–2Cr–2Nb alloy: Microstructure and mechanical properties investigation, Intermetallics. 19 (2011) 776–781. doi:10.1016/J.INTERMET.2010.11.017.

[9]   G. Marchese, S. Parizia, M. Rashidi, A. Saboori, D. Manfredi, D. Ugues, M. Lombardi, E. Hryha, S. Biamino, The role of texturing and microstructure evolution on the tensile behavior of heat-treated Inconel 625 produced via laser powder bed fusion, Mater. Sci. Eng. A. 769 (2020) 138500. doi:https://doi.org/10.1016/j.msea.2019.138500.

[10]   A. Saboori, A. Aversa, G. Marchese, S. Biamino, M. Lombardi, P. Fino, Application of Directed Energy Deposition-Based Additive Manufacturing in Repair, Appl. Sci. 9 (2019). doi:10.3390/app9163316.

[11]   H. Galarraga, D.A. Lados, R.R. Dehoff, M.M. Kirka, P. Nandwana, Effects of the microstructure and porosity on properties of Ti-6Al-4V ELI alloy fabricated by electron beam melting (EBM), Addit. Manuf. 10 (2016) 47–57. doi:https://doi.org/10.1016/j.addma.2016.02.003.

[12]   A. Aversa, A. Saboori, E. Librera, M. [de Chirico], S. Biamino, M. Lombardi, P. Fino, The Role of Directed Energy Deposition Atmosphere Mode on the Microstructure and Mechanical Properties of 316L Samples, Addit. Manuf. (2020) 101274. doi:https://doi.org/10.1016/j.addma.2020.101274.

[13]   A. Saboori, G. Piscopo, M. Lai, A. Salmi, S. Biamino, An investigation on the effect of deposition pattern on the microstructure, mechanical properties and residual stress of 316L produced by Directed Energy Deposition, Mater. Sci. Eng. A. 780 (2020) 139179. doi:https://doi.org/10.1016/j.msea.2020.139179.

[14]   R. Barros, F.J.G. Silva, R.M. Gouveia, A. Saboori, G. Marchese, S. Biamino, A. Salmi, E. Atzeni, Laser powder bed fusion of inconel 718: Residual stress analysis before and after heat treatment, Metals (Basel). 9 (2019). doi:10.3390/met9121290.

[15]   X. Zhao, S. Li, M. Zhang, Y. Liu, T.B. Sercombe, S. Wang, Y. Hao, R. Yang, L.E. Murr, Comparison of the microstructures and mechanical properties of Ti–6Al–4V fabricated by selective laser melting and electron beam melting, Mater. Des. 95 (2016) 21–31. doi:https://doi.org/10.1016/j.matdes.2015.12.135.

[16]   A. Saboori, D. Gallo, S. Biamino, P. Fino, M. Lombardi, An overview of additive manufacturing of titanium components by directed energy deposition: Microstructure and mechanical properties, Appl. Sci. 7 (2017). doi:10.3390/app7090883.

[17]   M. Aristizabal, P. Jamshidi, A. Saboori, S.C. Cox, M.M. Attallah, Laser powder bed fusion of a Zr-alloy: Tensile properties and biocompatibility, Mater. Lett. 259 (2020) 126897. doi:https://doi.org/10.1016/j.matlet.2019.126897.

[18]   A. Saboori, A. Aversa, F. Bosio, E. Bassini, E. Librera, M. De Chirico, S. Biamino, D. Ugues, P. Fino, M. Lombardi, An investigation on the effect of powder recycling on the microstructure and mechanical properties of AISI 316L produced by Directed Energy Deposition, Mater. Sci. Eng. A. (2019) 138360. doi:https://doi.org/10.1016/j.msea.2019.138360.

[19]   X. Tan, Y. Kok, Y.J. Tan, M. Descoins, D. Mangelinck, S.B. Tor, K.F. Leong, C.K. Chua, Graded microstructure and mechanical properties of additive manufactured Ti–6Al–4V via electron beam melting, Acta Mater. 97 (2015) 1–16. doi:http://dx.doi.org/10.1016/j.actamat.2015.06.036.

[20]   C. De Formanoir, S. Michotte, O. Rigo, L. Germain, S. Godet, Electron beam melted Ti–6Al–4V: Microstructure, texture and mechanical behavior of the as-built and heat-treated material, Mater. Sci. Eng. A. 652 (2016) 105–119.

[21]   J. Jiang, P. Hooper, N. Li, Q. Luan, C. Hopper, M. Ganapathy, J. Lin, An integrated method for net-shape manufacturing components combining 3D additive manufacturing and compressive forming processes, Procedia Eng. 207 (2017) 1182–1187. doi:https://doi.org/10.1016/j.proeng.2017.10.1050.

[22]   E.D. Roush, P.A. Kobryn, S.L. Semiatin, Anisotropy of plastic flow and microstructure evolution during hot working of laser-deposited Ti–6Al–4V, Scr. Mater. 45 (2001) 717–724. doi:https://doi.org/10.1016/S1359-6462(01)01084-3.

[23]   I. Sizova, M. Bambach, Hot workability and microstructure evolution of pre-forms for forgings produced by additive manufacturing, Procedia Eng. 207 (2017) 1170–1175. doi:https://doi.org/10.1016/j.proeng.2017.10.1048.

[24]   X. Qiu, N. ul Haq Tariq, L. Qi, Y. Zan, Y. Wang, J. Wang, H. Du, T. Xiong, In-situ Sip/A380 alloy nano/micro composite formation through cold spray additive manufacturing and subsequent hot rolling treatment: Microstructure and mechanical properties, J. Alloys Compd. 780 (2019) 597–606. doi:https://doi.org/10.1016/j.jallcom.2018.11.399.

[25]   A. Mostafa, D. Shahriari, I.P. Rubio, V. Brailovski, M. Jahazi, M. Medraj, Hot compression behavior and microstructure of selectively laser-melted IN718 alloy, Int. J. Adv. Manuf. Technol. 96 (2018) 371–385. doi:10.1007/s00170-017-1522-4.

[26]   M. Bambach, I. Sizova, F. Silze, M. Schnick, Hot workability and microstructure evolution of the nickel-based superalloy Inconel 718 produced by laser metal deposition, J. Alloys Compd. 740 (2018) 278–287. doi:https://doi.org/10.1016/j.jallcom.2018.01.029.

[27]   T. Seshacharyulu, S.C. Medeiros, W.G. Frazier, Y.V.R.K. Prasad, Hot working of commercial Ti–6Al–4V with an equiaxed α–β microstructure: materials modeling considerations, Mater. Sci. Eng. A. 284 (2000) 184–194. doi:https://doi.org/10.1016/S0921-5093(00)00741-3.

[28]   A. Momeni, S.M. Abbasi, Effect of hot working on flow behavior of Ti–6Al–4V alloy in single phase and two phase regions, Mater. Des. 31 (2010) 3599–3604. doi:https://doi.org/10.1016/j.matdes.2010.01.060.

[29]   B. Guo, S.L. Semiatin, J.J. Jonas, S. Yue, Dynamic transformation of Ti–6Al–4V during torsion in the two-phase region, J. Mater. Sci. 53 (2018) 9305–9315. doi:10.1007/s10853-018-2237-0.

[30]   J. Porntadawit, V. Uthaisangsuk, P. Choungthong, Modeling of flow behavior of Ti–6Al–4V alloy at elevated temperatures, Mater. Sci. Eng. A. 599 (2014) 212–222.

doi:https://doi.org/10.1016/j.msea.2014.01.064.

[31]   Y. Zhao, J. Sun, J. Li, Y. Yan, P. Wang, A comparative study on Johnson-Cook and modified Johnson-Cook constitutive material model to predict the dynamic behavior laser additive manufacturing FeCr alloy, J. Alloys Compd. 723 (2017) 179–187. doi:https://doi.org/10.1016/j.jallcom.2017.06.251.

[32]   P. Tao, J. Zhong, H. Li, Q. Hu, S. Gong, Q. Xu, Microstructure, Mechanical Properties, and Constitutive Models for Ti–6Al–4V Alloy Fabricated by Selective Laser Melting (SLM), Metals (Basel). 9 (2019). doi:10.3390/met9040447.

[33]   M. Bambach, I. Sizova, O. Geisen, O. Fergani, Comparison of the Hot Working Behavior of Wrought, Selective Laser Melted and Electron Beam Melted Ti-6Al-4V, in: THERMEC 2018, Trans Tech Publications Ltd, 2019: pp. 2030–2036. doi:10.4028/www.scientific.net/MSF.941.2030.

[34]   H. Mirzadeh, A Simplified Approach for Developing Constitutive Equations for Modeling and Prediction of Hot Deformation Flow Stress, Metall. Mater. Trans. A. 46 (2015) 4027–4037. doi:10.1007/s11661-015-3006-1.

[35]   Y.C. Lin, X.-M. Chen, A critical review of experimental results and constitutive descriptions for metals and alloys in hot working, Mater. Des. 32 (2011) 1733–1759. doi:https://doi.org/10.1016/j.matdes.2010.11.048.

[36]   P.M. Souza, H. Beladi, R.P. Singh, P.D. Hodgson, B. Rolfe, An Analysis on the Constitutive Models for Forging of Ti6Al4V Alloy Considering the Softening Behavior, J. Mater. Eng. Perform. 27 (2018) 3545–3558. doi:10.1007/s11665-018-3402-y.

[37]   M. Hu, L. Dong, Z. Zhang, X. Lei, R. Yang, Y. Sha, Correction of Flow Curves and Constitutive Modelling of a Ti-6Al-4V Alloy, Metals (Basel). 8 (2018). doi:10.3390/met8040256.

[38]   Y.C. Lin, D.-D. Chen, M.-S. Chen, X.-M. Chen, J. Li, A precise BP neural network-based online model predictive control strategy for die forging hydraulic press machine, Neural Comput. Appl. 29 (2018) 585–596. doi:10.1007/s00521-016-2556-5.

[39]   S. Mandal, P. V Sivaprasad, P. Barat, B. Raj, An Overview of Neural Network Based Modeling in Alloy Design and Thermomechanical Processing of Austenitic Stainless Steels, Mater. Manuf. Process. 24 (2009) 219–224. doi:10.1080/10426910802612361.

[40]   H. Mirzadeh, J.M. Cabrera, A. Najafizadeh, Modeling and Prediction of Hot Deformation Flow Curves, Metall. Mater. Trans. A. 43 (2012) 108–123. doi:10.1007/s11661-011-0836-3.

[41]   C. [de Formanoir], S. Michotte, O. Rigo, L. Germain, S. Godet, Electron beam melted Ti–6Al–4V: Microstructure, texture and mechanical behavior of the as-built and heat-treated material, Mater. Sci. Eng. A. 652 (2016) 105–119. doi:https://doi.org/10.1016/j.msea.2015.11.052.

[42]   M.A. Galindo-Fernández, K. Mumtaz, P.E.J. Rivera-Díaz-del-Castillo, E.I. Galindo-Nava, H. Ghadbeigi, A microstructure sensitive model for deformation of Ti-6Al-4V describing Cast-and-Wrought and Additive Manufacturing morphologies, Mater. Des. 160 (2018) 350–362. doi:https://doi.org/10.1016/j.matdes.2018.09.028.

[43]   Y.C. Lin, X.-Y. Jiang, C. Shuai, C.-Y. Zhao, D.-G. He, M.-S. Chen, C. Chen, Effects of initial microstructures on hot tensile deformation behaviors and fracture characteristics of Ti-6Al-4V alloy, Mater. Sci. Eng. A. 711 (2018) 293–302. doi:https://doi.org/10.1016/j.msea.2017.11.044.

[44]   J.S. Jha, S.P. Toppo, R. Singh, A. Tewari, S.K. Mishra, Flow stress constitutive relationship between lamellar and equiaxed microstructure during hot deformation of Ti-6Al-4V, J. Mater. Process. Technol. 270 (2019) 216–227. doi:https://doi.org/10.1016/j.jmatprotec.2019.02.030.

[45]   A. Saboori, M. Dadkhah, M. Pavese, D. Manfredi, S. Biamino, P. Fino, Hot deformation behavior of Zr-1%Nb alloy: Flow curve analysis and microstructure observations, Mater. Sci. Eng. A. 696 (2017) 366–373. doi:http://dx.doi.org/10.1016/j.msea.2017.04.049.

[46]   T. Sheppard, J. Norley, Deformation characteristics of Ti–Al–V, Mater. Sci. Technol. 4 (1988) 903–908. doi:10.1179/mst.1988.4.10.903.

[47]   P. Honarmandi, M. Aghaie-Khafri, Hot Deformation Behavior of Ti–6Al–4V Alloy in β Phase

Field and Low Strain Rate, Metallogr. Microstruct. Anal. 2 (2013) 13–20. doi:10.1007/s13632-012-0052-6.

[48] T. Seshacharyulu, S.C. Medeiros, W.G. Frazier, Y.V.R.K. Prasad, Microstructural mechanisms during hot working of commercial grade Ti–6Al–4V with lamellar starting structure, Mater. Sci. Eng. A. 325 (2002) 112–125. doi:https://doi.org/10.1016/S0921-5093(01)01448-4.

[49] T. Seshacharyulu, S.C. Medeiros, J.T. Morgan, J.C. Malas, W.G. Frazier, Y.V.R.. Prasad, Hot deformation and microstructural damage mechanisms in extra-low interstitial (ELI) grade Ti–6Al–4V, Mater. Sci. Eng. A. 279 (2000) 289–299. doi:https://doi.org/10.1016/S0921-5093(99)00173-2.

[50] J. Luo, M. Li, H. Li, W. Yu, Effect of the strain on the deformation behavior of isothermally compressed Ti–6Al–4V alloy, Mater. Sci. Eng. A. 505 (2009) 88–95. doi:https://doi.org/10.1016/j.msea.2008.11.001.

[51] R. Ding, Z.X. Guo, A. Wilson, Microstructural evolution of a Ti–6Al–4V alloy during thermomechanical processing, Mater. Sci. Eng. A. 327 (2002) 233–245. doi:https://doi.org/10.1016/S0921-5093(01)01531-3.

[52] F.J. Humphreys, M. Hatherly, Chapter 2 - The Deformed State, in: F.J. Humphreys, M. Hatherly (Eds.), Recryst. Relat. Annealing Phenom. (Second Ed., Second Edi, Elsevier, Oxford, 2004: pp. 11–II. doi:https://doi.org/10.1016/B978-008044164-1/50006-2.

[53] X. Fan, Q. Li, A. Zhao, Y. Shi, W. Mei, The Effect of Initial Structure on Phase Transformation in Continuous Heating of a TA15 Titanium Alloy, Metals (Basel). 7 (2017). doi:10.3390/met7060200.

[54] M. Neikter, P. Åkerfeldt, R. Pederson, M.-L. Antti, Microstructure characterisation of Ti-6Al-4V from different additive manufacturing processes, {IOP} Conf. Ser. Mater. Sci. Eng. 258 (2017) 12007. doi:10.1088/1757-899x/258/1/012007.

[55] I. Ghamarian, B. Hayes, P. Samimi, B.A. Welk, H.L. Fraser, P.C. Collins, Developing a phenomenological equation to predict yield strength from composition and microstructure in β processed Ti-6Al-4V, Mater. Sci. Eng. A. 660 (2016) 172–180. doi:https://doi.org/10.1016/j.msea.2016.02.052.

[56] H.J. McQueen, N.D. Ryan, Constitutive analysis in hot working, Mater. Sci. Eng. A. 322 (2002) 43–63. doi:https://doi.org/10.1016/S0921-5093(01)01117-0.

[57] S. Mandal, V. Rakesh, P. V Sivaprasad, S. Venugopal, K. V Kasiviswanathan, Constitutive equations to predict high temperature flow stress in a Ti-modified austenitic stainless steel, Mater. Sci. Eng. A. 500 (2009) 114–121. doi:http://dx.doi.org/10.1016/j.msea.2008.09.019.

[58] F.A. Slooff, J. Zhou, J. Duszczyk, L. Katgerman, Constitutive analysis of wrought magnesium alloy Mg–Al4–Zn1, Scr. Mater. 57 (2007) 759–762. doi:http://dx.doi.org/10.1016/j.scriptamat.2007.06.023.

[59] A.K. Mukherjee, An examination of the constitutive equation for elevated temperature plasticity, Mater. Sci. Eng. A. 322 (2002) 1–22. doi:https://doi.org/10.1016/S0921-5093(01)01115-7.

[60] T.G. Langdon, An analysis of flow mechanisms in high temperature creep and superplasticity, Mater. Trans. 46 (2005) 1951–1956.

[61] H. Mirzadeh, J.M. Cabrera, A. Najafizadeh, Constitutive relationships for hot deformation of austenite, Acta Mater. 59 (2011) 6441–6448. doi:https://doi.org/10.1016/j.actamat.2011.07.008.

[62] J.M. Cabrera, A. Al Omar, J.M. Prado, J.J. Jonas, Modeling the flow behavior of a medium carbon microalloyed steel under hot working conditions, Metall. Mater. Trans. A. 28 (1997) 2233–2244. doi:10.1007/s11661-997-0181-8.

[63] S. Saadatkia, H. Mirzadeh, J.-M. Cabrera, Hot deformation behavior, dynamic recrystallization, and physically-based constitutive modeling of plain carbon steels, Mater. Sci. Eng. A. 636 (2015) 196–202. doi:https://doi.org/10.1016/j.msea.2015.03.104.

[64] D.A. Porter, K.E. Easterling, Phase Transformations in Metals and Alloys, 2nd ed., Chapman & Hall, 1992.

[65] H. Mirzadeh, Constitutive modeling of commercial pure titanium during hot deformation in alpha

and beta phase fields, Indian J. Eng. Mater. Sci. 23 (2016) 60–64.